ARTICLE OPEN

Check for updates

Single-nucleus transcriptomics reveals disrupted pathways in the prefrontal cortex of *Scn2a*-deficient mice

Ye-Eun Yoo[1,2,9], Zaiyang Zhang[1,2,9], Purba Mandal[2,3], Zhengkuan Tang[1,2], Jingliang Zhang[1,2], Xiaoling Chen[1,2], Morgan Robinson[1,2], Muriel Eaton[1,2], Brody Deming[1,2], Manasi Halurkar[1,2], Harish Kothandaraman[4], Luke C. Dabin[5], Boyu Jiang[2,3], Hongyu Gao[6], Chongli Yuan[7], Nadia Lanman[4,8], Yunlong Liu[6], Jungsu Kim[5], Priyanka Baloni[2,3] and Yang Yang[1,2]✉

© The Author(s) 2026

Loss-of-function variants in *SCN2A*, which encodes the $Na_V1.2$ sodium channel critical for action potential initiation and backpropagation, are associated with autism spectrum disorder (ASD) and epilepsy. To investigate *SCN2A* deficiency–related phenotypes, we developed a preclinical mouse model with severe $Na_V1.2$ deficiency, which exhibits robust behavioral abnormalities related to autism and epilepsy. However, the neuronal populations and molecular alterations in the mouse model have not been investigated at single-cell resolution. In this study, we performed single-nucleus RNA sequencing (snRNA-seq) in wild-type (WT), homozygous *Scn2a*-deficient (HOM), and *Scn2a*-restored HOM (HOM-FlpO) mice. We then examined how *Scn2a* expression levels affect cellular composition and gene expression profiles in the medial prefrontal cortex (mPFC), a brain region implicated in ASD. Intriguingly, we observed an increased population of immature GABAergic neurons in adult HOM mice, whereas this population is nearly absent in adult WT mice. Differential expression analysis of GABAergic and glutamatergic neurons across genotypes also revealed widespread changes in genes associated with neurotransmitter regulation and synapse organization. Analysis of the HOM-FlpO data identified genes that were significantly altered in HOM mice and were restored toward WT levels following adult *Scn2a* restoration. Together, these results indicate that reduced *Scn2a* expression disrupts global transcriptomic profiles across multiple neural cell types, providing insight into cell–type–specific mechanisms underlying *SCN2A*-related disorders.

Translational Psychiatry (2026)16:592 ; https://doi.org/10.1038/s41398-026-04348-0

INTRODUCTION

The *SCN2A* gene, encoding voltage-gated sodium channels $Na_V1.2$, has a critical role in regulating neuronal excitability [1–3]. It is mainly expressed in the axon initial segment (AIS) and dendrites of neurons in the central nervous system, where it contributes to the generation and backpropagation of action potentials [4–6]. Several genetic studies have identified *SCN2A* as one of the most prominent risk genes for autism spectrum disorders (ASDs) [7–10]. Mutations in *SCN2A* disrupt neuronal excitability, leading to atypical neurodevelopment, impaired social and cognitive function, and epileptic seizures [11–13]. In particular, patients with loss-of-function *SCN2A* mutations (i.e., *Scn2a* deficiency) often present with severe autism and developmental delays [2, 14, 15]. To date, the precise cellular disturbance underlying *SCN2A* deficiency–related disorders remains unknown.

To study *Scn2a* deficiency, we previously developed a preclinical *Scn2a* gene trap mouse model, which displays pronounced behavioral and cellular deficits, including social impairment and hyperexcitability in pyramidal neurons of the medial prefrontal cortex (mPFC) [16, 17]. The mPFC is an important brain region involved in higher cognitive functions, such as social interaction, and has been implicated in autism and developmental delays [18, 19]. A diverse array of neuronal subtypes in the mPFC integrates inputs from multiple brain regions and projects to subcortical structures, forming circuits that support a wide range of executive functions [20–23]. It is evident that proper cell-type composition in the mPFC is essential for information integration, and dysfunction in this region contributes to multiple neurodevelopmental and neuropsychiatric disorders [24–26]. Still, it remains unclear which neural cell types are most affected by *Scn2a* deficiency and what specific gene expression changes occur within this critical brain region. Characterizing cell–type–specific molecular effects of *Scn2a* deficiency is critical for elucidating the mechanisms of *SCN2A*-related disorders and identifying therapeutic targets. Clinical studies in ASD suggest the existence of a critical period during which interventions may be most effective [27]. However, many individuals continue to exhibit persistent symptoms into adulthood. Determining whether molecular and cellular deficits can be rescued later in life is therefore of substantial translational importance, as it directly addresses the reversibility of pathology beyond early developmental stages. Interestingly, our

[1]Borch Department of Medicinal Chemistry and Molecular Pharmacology, College of Pharmacy, Purdue University, West Lafayette, IN, USA. [2]Purdue Institute for Integrative Neuroscience, Purdue University, West Lafayette, IN, USA. [3]School of Health Sciences, Purdue University, West Lafayette, IN, USA. [4]Purdue Institute for Cancer Research, West Lafayette, IN 47907, USA. [5]Department of Medical and Molecular Genetics, Indiana University School of Medicine, Indianapolis, IN 46202, USA. [6]Center for Medical Genomics, Indiana University School of Medicine, Indianapolis, IN, USA. [7]Davidson School of Chemical Engineering, West Lafayette, IN, USA. [8]Department of Comparative Pathobiology, College of Veterinary Medicine, Purdue University, West Lafayette, IN, USA. [9]These authors contributed equally: Ye-Eun Yoo, Zaiyang Zhang. ✉email: yangyang@purdue.edu

Received: 13 November 2025 Revised: 17 July 2026 Accepted: 24 July 2026
Published online: 31 July 2026

previous results demonstrated that global restoration of *Scn2a* expression in adult *Scn2a*-deficient mice significantly rescues social deficits and normalizes neuronal hyperexcitability [17, 28]. However, how single-cell gene expression profiles are restored following *Scn2a* re-expression remains unclear.

To investigate cell-type-specific molecular and cellular changes induced by *Scn2a* deficiency, we performed single-nucleus RNA sequencing (snRNA-seq) for the mPFC of the WT mice, homozygous *Scn2a*-deficient (HOM) mice, and HOM mice with FlpO-induced restored *Scn2a* (WT, HOM, HOM-FlpO, hereafter). We observed an unexpected increase in immature GABAergic neurons in HOM mice. Differentially expressed genes (DEGs) between HOM and WT were predominantly associated with synaptic transmission and cell signaling-related pathways. Finally, cell-cell communication network analysis revealed that increased intercellular communication in HOM mPFC was ameliorated by FlpO-induced *Scn2a* restoration. This study identifies molecular alterations by comparing single-cell transcriptomic differences between WT and *Scn2a*-deficient mice, providing insight into cell-type–specific gene expression changes associated with congenital *Scn2a* deficiency.

METHODS

Animal model

C57BL/6N-*Scn2a*^{tm1aNarl}/Narl (*Scn2a*$^{+/gt}$) mice were generated and characterized as previously described [16]. Briefly, heterozygous (HET, *Scn2a*$^{+/gt}$) mice were bred to obtain homozygous (HOM, *Scn2a*$^{gt/gt}$) and wild-type (WT, *Scn2a*$^{+/+}$) littermates for experiments. Mice were group-housed (3–5 per cage) on vented cage racks with a 12-h light/dark cycle. Food and water were given *ad libitum*. All animal procedures were approved by the Purdue University Institutional Animal Care and Use Committee under protocol number IACUC 1806001760 and were conducted in accordance with the National Institutes of Health guidelines for laboratory animals.

Adeno-associated virus (AAV) transduction

For the *Scn2a* HOM-FlpO group, AAV-PHP.eB vectors were prepared and systemically delivered to mice as previously described [17]. 3-5-month-old mice received 2×10^{11} viral particles of AAV-FlpO (PHP.eB-EF1a-mCherry-IRES-Flpo-WPRE-hGH) or control AAV-mCherry virus (PHP.eB-Ef1a-DO-mCherry-WPRE-pA) via tail vein injection.

Library preparation and single-nucleus RNA sequencing (snRNA-seq)

Frozen prefrontal cortex brain tissues from four replicates, including two females and two males per group (WT, HOM, HOM-FlpO), were used. Mice were deeply anesthetized with ketamine/xylazine (100/10 mg/kg, intraperitoneal injection), and brains were rapidly extracted and flash-frozen in liquid nitrogen. Coronal brain sections containing the medial prefrontal cortex (mPFC) were prepared, and the mPFC regions were dissected using a cold biopsy punch as previously described [29]. The tissue samples were homogenized in the chilled lysis buffer (10 mM Tris-HCl, pH 7.5, 10 mM NaCl, 3 mM MgCl2, 0.1% Nonidet P40 Substitute, 1 mM DTT, 0.2 U/µl RNase inhibitor) using a Dounce homogenizer. Lysates were centrifuged and filtered with a 40 µm cell strainer. Dissociated nuclei were resuspended in PBS containing BSA and RNase inhibitor, and then purified by cell sorter for downstream library preparation. snRNA-seq libraries were generated using Chromium Next GEM Single Cell 3′ Reagent Kits v3.1 (10X Genomics), following the manufacturer's instructions. Approximately 6000 nuclei per sample were targeted for capture on the Chromium platform. Final libraries were sequenced on an Illumina NovaSeq 6000, with a targeted sequencing depth of ~60,000 reads per nucleus.

Processing of single-nucleus RNA sequencing data

The sequencing data were processed via the standard pipeline of the Cell Ranger single-cell software suite 6.1.1 (10x Genomics). The FASTQ files generated by the pipeline were aligned to the mouse reference genome (mm10) and used to create the gene expression matrix based on counts of unique molecular identifiers (UMIs) assigned to each transcript by Cell Ranger. The filtered gene expression matrices were used for subsequent downstream analysis.

Single-nucleus RNA sequencing data analysis

The gene expression matrices were further analyzed using the Scanpy package [30] (v1.10.2). To remove low-quality nuclei, cells with fewer than 500 unique genes and more than 6000 genes were removed. To exclude cytoplasmic transcripts and avoid biases introduced during nuclear isolation and ultracentrifugation, cells with greater than 10% of reads mapping to mitochondrial genes were removed. The dataset was further filtered for doublets using Scrublet package [31] (v0.2.3) using the default parameters. A total of 47,291 cells were retained for downstream analysis, including 14,204 cells from WT, 15,097 cells from HOM, and 17,990 cells from HOM-FlpO.

The filtered data were normalized by total counts per cell using the 'scanpy.pp.normalize_per_cell' function, followed by log-transformation with the 'scanpy.pp.log1p' function (natural log, log(x + 1) transformation applied to the data matrix). To address potential batch effects across samples, we selected the top 3000 highly variable genes using 'scanpy.pp.highly_variable_genes' and used them for principal component analysis (PCA, 50 PCs) and batch-balanced k-nearest neighbors (BBKNN).

The processed data were then converted into Seurat [32, 33] (v5.0.1) for visualization. Local neighborhoods were computed with 'FindNeighbors' (dimension = 17), followed by clustering with 'FindClusters' (resolution = 0.7). Dimensional reduction was visualized using the uniform manifold approximation and projection (UMAP) algorithm. scCustomize [34] (v2.1.2) package in R (v4.3.2) was applied to generate dot plots and feature plots.

Cell-type identification

An h5ad file was created using the anndata (v0.10.5) package in R and then mapped to a reference 10x Whole Mouse Brain (CCN20230722). The hierarchical mapping algorithm in MapMyCells (RRID: SCR_024672; https://portal.brain-map.org/atlases-and-data/bkp/mapmycells) [35, 36] was chosen to get the broad cell class names, subclass names, and their respective bootstrap probability, which were aligned with the cell barcodes of the Seurat object. As an initial quality control step, cells expressing more than the 99th percentile of genes were removed, and classes with fewer than 10 cells were excluded. Namely, IT (intratelencephalic projecting)-ET (extratelencephalic projecting)-Glut (Glutamatergic neurons), CR (Cajal–Retzius) Glut, NP (near-projecting)-CT (corticothalamic projecting)-L6b Glut, CTX (Cortex)-MGE (medial ganglionic eminence) Gaba (GABAergic neurons), CTX-CGE (caudal ganglionic eminence) Gaba, IMN (immature) Gaba, Astrocytes, OPC (Oligodendrocyte progenitor cells)-Oligo (Oligodendrocytes), OEC (Olfactory ensheathing cells), Vascular and Immune cells. After filtering, cells were manually grouped into the first three main categories—excitatory subtypes, inhibitory subtypes, and non-neuronal cells—based on relevant marker genes and the broad class names provided by the 10x Whole Mouse Brain reference.

For subclustering, dimensionality was determined by identifying the first principal component at which the cumulative explained variance exceeded 90%. Clustering resolution was selected by evaluating resolution-dependent patterns using the Clustree package [37] (v0.5.1). Excitatory cells were subclustered into 9 main groups (15 dimensions, resolution = 0.2): L2/3 IT, L4/5 IT, L5 IT, L6 IT, L5/6 IT, L5 ET, L6 CT, L5 NP, and CR Glut. Inhibitory neurons were subclustered into 10 groups (12 dimensions, resolution = 0.1): Lamp5 Gaba, Sncg Gaba, Vip Gaba, Sst Gaba, Pvalb Gaba, IMN Frmd7 Gaba 1, IMN Frmd7 Gaba 2, IMN Thsd7b Gaba, IMN Trdn Gaba, and IMN Dopa-Gaba. Non-neuronal (NN) cells were subclustered into 6 groups (18 dimensions, resolution = 0.1): Microglia, Astrocytes, Vascular, Oligodendrocyte Progenitor Cell (OPC), Oligodendrocytes, and Olfactory Ensheathing Cell (OEC).

Spearman correlation analysis

Normalized expression matrices were obtained for WT and HOM, and *Meis2* expression values were extracted for analysis. Spearman correlation between *Meis2* and all other genes was calculated using the cor() function in R (v4.3.2). Genes with a correlation coefficient ≥ 0.3 were considered significantly correlated and retained for further analysis. Correlation values were visualized using a bar plot generated with ggplot2.

Predicting RNA velocity using scVelo

RNA velocity was estimated using the scVelo package (v0.3.2) [38]. The spliced and unspliced mRNA counts are identified using Velocyto (v0.17.17) [39] with default settings. The first and second moments of spliced and unspliced counts were computed using the scVelo function scvelo.pp.moments with n_neighbors set to 30. The genes that explain the

resulting vector field and inferred lineages were identified by scv.tl.rank_velocity_genes.

The velocity vectors were calculated using the scvelo.tl.velocity function, employing the stochastic model of RNA velocity. Velocity confidence intervals were estimated using the scvelo.tl.velocity_confidence function. Velocity embeddings were visualized by projecting the velocity vectors onto UMAP, using the scvelo.pl.velocity_embedding_stream and scvelo.pl.velocity_embedding_grid functions.

Differential expression analysis and enrichment analysis

To identify genotype-associated differentially expressed genes (DEGs) between each genotype, the scanpy.tl.rank_genes_groups() function was used to identify the most variable genes ($n = 3000$), testing differences in expression between groups of cells. A non-parametric two-sided Wilcoxon rank-sum test was performed at the single-cell level to calculate the log-scale fold change and adjusted p-value for each gene. Only DEGs with an absolute average log fold change > 0.5 and an adjusted p-value < 0.05 (Benjamini-Hochberg procedure) were considered significant. ClueGO [40] (v2.5.10). One of the modules in Cytoscape (v3.10.2), was used for depicting enriched ontologies for DEGs. Protein-protein interactions between DEGs were illustrated by STRING (v2.2.0) analysis [41] in Cytoscape.

Cell-cell interaction analysis

CellPhoneDB v5 [42] was used to infer potential ligand-receptor interactions between cell subsets. For each genotype, CellPhoneDB was run separately on the corresponding h5ad file. To focus on biologically relevant interactions, only differentially expressed significant genes (Benjamini-Hochberg procedure, FDR < 0.05) were included. These DEGs were used to restrict ligand-receptor pairing, ensuring that predicted interactions reflected genotype-specific transcriptional changes. The predicted interactions were further processed to show the mean of interaction scores, and then the top 5% of interactions based on mean expression level were extracted to plot using the OmicVerse package (v1.6.8) [43].

RNAscope

After mice were perfused with 4% paraformaldehyde (PFA), brains were removed and post-fixed with 4% PFA overnight. Brains were transferred to 30% sucrose in 1X PBS, then immersed in O.C.T compound (Sakura Finetek, #4583). 30 µm brain tissue sections were generated on a cryostat. RNAscope was performed following the manufacturer's protocol for the RNAscope Multiplex Fluorescent Detection Reagents v2 kit (ACD, #323110). The Gad1 (#400951-C2) and Meis2 probes (#436371) were used for co-localization studies. Quantification of RNAscope signals was done using QuPath 0.5.1 [44].

Statistics

Statistical analyses for each experiment were performed in R (v4.3.3) or GraphPad Prism (v10.1.2). A Shapiro-Wilk normality test was performed to assess normality. Two-tailed Student's t-tests (parametric) or unpaired two-tailed Mann-Whitney U-tests (non-parametric) were used for single comparisons between two groups. All data were expressed as mean ± SEM, with statistical significance determined at p values < 0.05. In detail, $p \geq 0.05$ is indicated as ns (no significance), $p < 0.05$ is indicated as one asterisk (*), $p < 0.01$ is indicated as two asterisks (**), and $p < 0.001$ is indicated as three asterisks (***) in all figures.

RESULTS

Cell type annotation of single-nucleus transcriptomes in the mPFC of Scn2a WT and HOM mice

To assess the impact of *Scn2a* deficiency on cell–type–specific molecular profiles in the mPFC, we performed single-nucleus RNA sequencing (snRNA-seq) on samples from WT and *Scn2a* HOM mice (Fig. 1A). We pooled two male and two female mice per genotype (4 WT and 4 HOM in total) and analyzed transcription from 29,301 nuclei after quality-control preprocessing (Figure S1A). For cell-type annotations, we applied MapMyCells [35] to leverage a comprehensive dataset of whole mouse brains from the Allen Brain Institute (Table S1). To evaluate the confidence of cell type assignments, we examined the bootstrapping probabilities generated by MapMyCells. This score reflects the proportion of bootstrap iterations in which an annotated cell maps to the same node in the reference cell-type taxonomy, providing a measure of classification reliability [35]. Most annotated cells exhibited a high bootstrapping probability score close to 1.0 (Figure S1B-D), indicating consistent and confident mapping across hierarchical levels of the taxonomy.

Uniform manifold approximation and projection (UMAP) dimensionality reduction and Leiden clustering of the transcriptomic datasets identified 25 subclasses (Fig. 1B) and 11 major cell classes (Fig. 1C). We observed that *Scn2a* is primarily expressed in intratelencephalic projecting (IT)-extratelencephalic projecting (ET) and near-projecting (NP)-corticothalamic projecting (CT)-L6b glutamatergic neurons, as well as in CTX-caudal ganglionic eminence (CGE) GABA neurons and CTX-medial ganglionic eminence (MGE) GABA neurons, consistent with known expression patterns of the *Scn2a* gene [45, 46] (Fig. 1D, Figure S1E).

We profiled the expression of established marker genes for major mPFC cell types: *Grin2a*, *Grin2b*, and *Slc17a7* for glutamatergic neurons; *Slc32a1* and *Gad1* for GABAergic neurons; *Cux2, Otof, Rorb, Nptx2*, and *Pou3f1* for IT-ET Glut neurons; *Fezf2, Tshz2, Syt6*, and *Sulf1* for NP-CT-L6b Glut neurons; and *Eomes* and *Ms4a15* for Cajal–Retzius (CR) Glut neurons. *Sncg, Lamp5*, and *Cnr1* were specifically expressed in CTX-CGE GABA neurons, while *Pvalb* and *Lhx6* were expressed in CTX-MGE GABA neurons (Fig. 1E). Notably, we observed a large subpopulation of *Meis2*+ immature GABAergic neurons, identified by co-expression of Meis2, Frmd7, Thsd7b, and Trdn, along with Gad1, which encodes GABA synthetase. In addition to neurons, we annotated non-neuronal (NN) cells based on marker gene expression: *Gjb6* for astrocytes, *Mog* for oligodendrocytes, *Pdgfra* for oligodendrocyte progenitor cells (OPCs), *Serpinf1* for vascular cells, *Cldn5* for olfactory ensheathing cells (OECs), and *Ctss* for microglia (Fig. 1E). Cell type annotations aligned with canonical markers, as shown in feature plots of gene expression across cell types for glutamatergic, GABAergic neurons, and non-neuronal cell types (Fig. 1F). Together, these results demonstrate the identification of distinct neuronal and non-neuronal subtypes in the mPFC using MapMyCells (RRID:SCR_024672) [35]. A complete list of class and subclass annotations for cell types is provided in Table S2.

Meis2+ immature GABAergic neurons are increased in the mPFC of Scn2a-deficient mice

As we observed *Meis2*+ immature GABAergic neurons expressing *Thsd7b*, *Trdn*, and *Frmd7* in our dataset, we sought to verify their expression in reference datasets. The Allen Brain Cell Atlas (https://knowledge.brain-map.org/abcatlas), which provides the single-cell spatial transcriptome of the adult mouse brain [35], confirmed high expression of these genes in OB-IMN-GABA neurons (Figure S2A), supporting that the population we identified corresponds to this subtype. OB-IMN-GABA neurons originate from the lateral ganglionic eminence (LGE) and migrate to the olfactory bulb (OB) [47, 48]. Although these neurons are primarily localized in the anterior olfactory nucleus (AON), small populations are also found in the striatum, lateral septal complex, and prelimbic/infralimbic regions of the mPFC (Figure S2B) [49]. Consistent with these reference data, *Meis2*+ immature GABAergic neurons have previously been reported in the mPFC of adult WT mice using snRNA-seq [35, 49].

Interestingly, UMAP analysis of our dataset revealed an increased IMN GABA neuron population in the mPFC of HOM mice compared to WT (Fig. 2A). A summary bar plot indicated that the proportion of IMN GABA neurons in mPFC was 2.99% in the WT but increased to 19.39% in the HOM, as highlighted in red (Fig. 2B). Moreover, *Meis2* is primarily expressed in the IMN GABA class and strongly co-expressed with the canonical GABAergic marker *Gad1* in our dataset (Fig. 1E). A comparison between

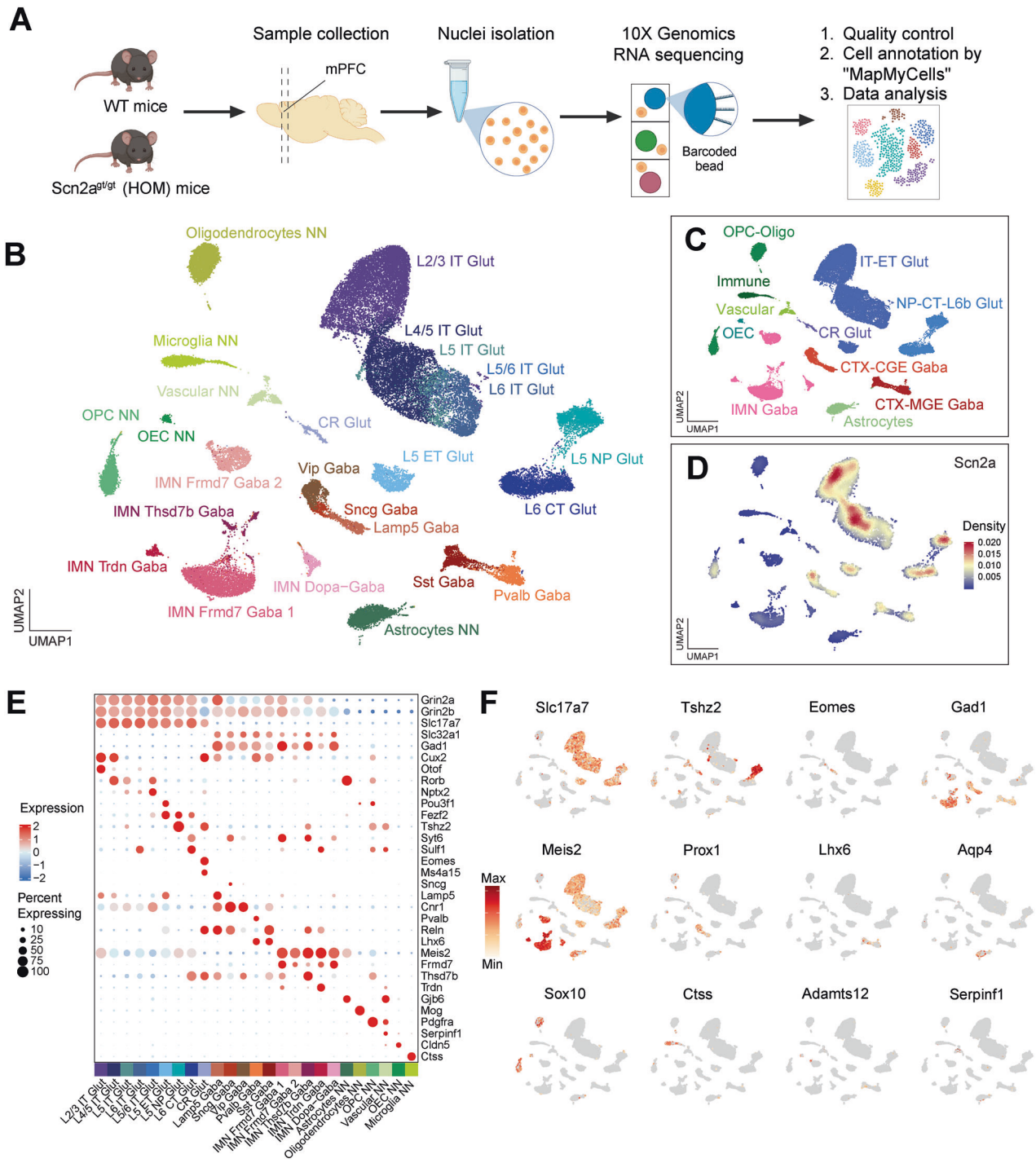


Fig. 1 MapMyCells annotation identifies major cell classes and subclasses in the mPFC of WT and *Scn2a*-deficient (HOM) mice. **A** Schematic of the experimental workflow. mPFC tissue was collected from WT and homozygous *Scn2a*-deficient (HOM) mice for snRNA-seq. Downstream analyses included quality control, cell type annotation using MapMyCells (RRID: SCR_024672), and transcriptomic profiling. **B** UMAP visualization of subclass-level annotations identified by MapMyCells across WT and HOM mPFC samples. **C** UMAP visualization of major cell classes annotated by MapMyCells in WT and HOM mPFC samples, including glutamatergic neurons (IT-ET Glut, NP-CT-L6b Glut, CR Glut), GABAergic neurons (CTX-CGE GABA, CTX-MGE GABA, IMN GABA), astrocytes, OPC-oligodendrocyte lineage cells, OECs, immune cells, and vascular cells. **D** Density plot showing *Scn2a* expression across annotated subclasses. *Scn2a* expression was detected in both glutamatergic and GABAergic neuronal populations. **E** Dot plot showing canonical marker gene expression across annotated subclasses. Marker genes include *Grin2a, Grin2b, Slc17a7, Cux2, Eomes, Ms4a15, Otof, Rorb, Nptx2, Pou3f1, Fezf2, Tshz2, Syt6*, and *Sulf1* for glutamatergic neurons; *Slc32a1, Gad1, Sncg, Lamp5, Cnr1, Pvalb, Reln, Lhx6, Meis2, Frmd7, Thsd7b*, and *Trdn* for GABAergic neurons; and *Gjb6, Mog, Pdgfra, Serpinf1, Ctss*, and *Cldn5* for non-neuronal populations. Color indicates scaled expression level, and dot size indicates the percentage of cells expressing each gene. **F** Feature plots showing the distribution of selected marker genes across neuronal and non-neuronal populations on the UMAP. Color intensity indicates relative expression level, and gray dots indicate cells with no detectable expression.

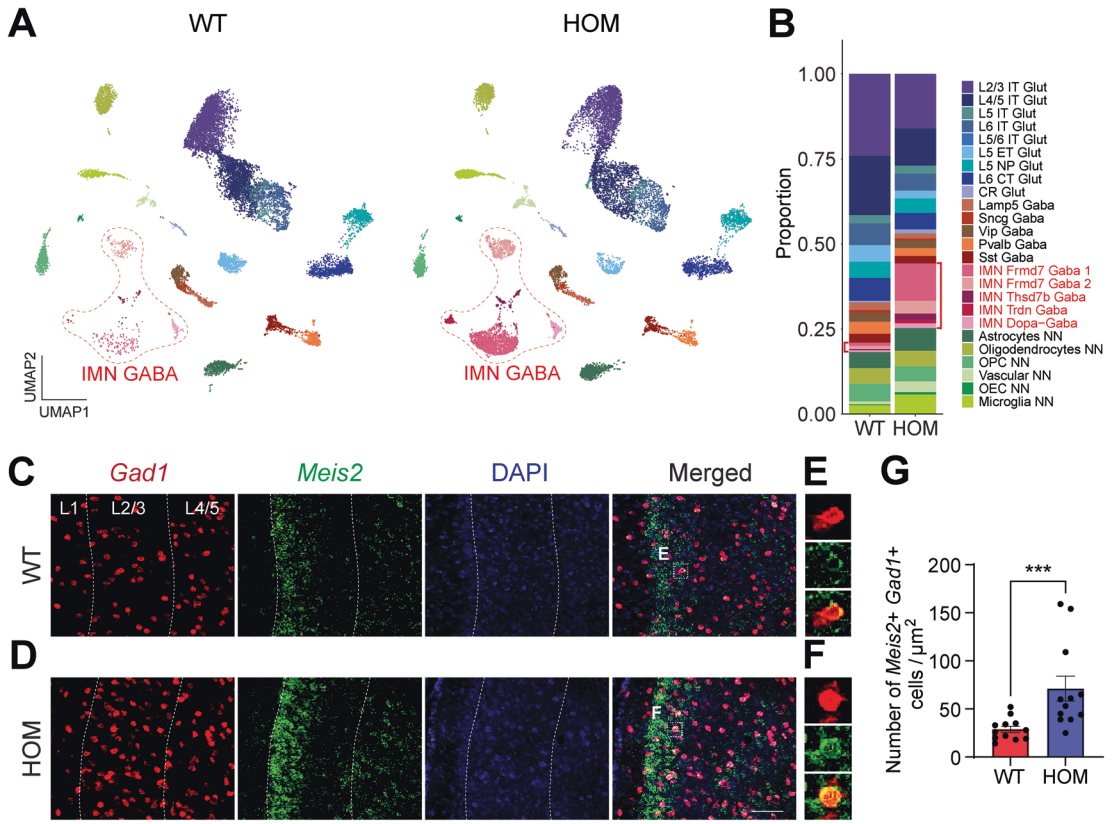


Fig. 2 ***Meis2*-expressing immature GABAergic neurons are increased in the mPFC of HOM mice. A** UMAP visualization comparing WT and HOM mPFC nuclei, highlighting genotype-associated differences in cell population distribution. IMN GABA neurons were increased in HOM mice. **B** Stacked bar plot showing the relative proportions of annotated cell classes in WT and HOM mice. The IMN GABA neuron population is highlighted in red. **C**, **D** Representative RNAscope images from WT (**C**) and HOM (**D**) mPFC. *Gad1* is shown in red, *Meis2* in green, and DAPI in blue. Cortical layers 1, 2/3, and 4/5 are indicated. Scale bar, 100 µm. **E**, **F** Magnified images showing cells co-expressing *Meis2* and *Gad1* in WT (**E**) and HOM (**F**) mPFC. **G** Quantification of *Meis2/Gad1* double-positive cells showing a significant increase in HOM mice compared with WT mice. ***$p < 0.001$, Mann–Whitney test after Shapiro–Wilk normality testing. WT: $n = 12$ sections from 4 animals; HOM: $n = 12$ sections from 4 animals.

genotypes showed that the number of *Meis2*+*Gad1*+ cells was higher in HOM mice than in WT (Figures S2C and 2G).

To validate the transcriptomic finding of increased *Meis2*+ IMN GABA neuron proportion in HOM mice, RNAScope in situ hybridization was performed using *Meis2* and *Gad1* probes. The RNAScope results in the mPFC region indicated that the *Meis2*+ IMN GABA neuron population increased in adult HOM mice compared to WT (Fig. 2C, D). Co-localization of *Gad1*+ and *Meis2*+ signals in each cell was also assessed (Fig. 2E, F). The number of cells expressing both *Meis2* and *Gad1* in the region of interest was higher in HOM compared to WT (mean = 28.8 cells/µm^2 for WT, mean = 71.1 cells/µm^2 for HOM, ***$p < 0.001$, Mann-Whitney U test) (Fig. 2G). The majority of the *Meis2*+ */Gad1*+ cells are accumulating in the superficial Layer 2/3, rather than uniformly across all cortical layers. The increased numbers of *Meis2*+ and *Gad1* + IMN GABA neurons observed in adult HOM mice, along with transcriptomic data, collectively indicate that congenital *Scn2a* deficiency alters GABAergic neuronal populations.

Genes altered in the transcriptomic profile of Scn2a-deficient mice are associated with neuronal development

A recent study reported that loss of *Scn2a* can affect neurogenesis and neuronal differentiation [50]. Therefore, we hypothesized that *Scn2a* deficiency induces developmental transcriptional changes, leading to aberrant cell-fate decisions and increased differentiation of immature GABAergic neurons in adulthood. To test this hypothesis, we employed scVelo, a computational method that models gene expression dynamics using snRNA-seq data [38]. Specifically, scVelo estimates RNA velocity, a vector representing the direction and speed of a cell's transcriptional state, by comparing levels of unspliced and spliced RNA transcripts (Table S3) [38, 51]. These velocity estimates are then used to infer latent time from pseudotemporal ordering, which places each cell along a developmental trajectory according to its transcriptional maturity [39, 52].

Integration of RNA velocity with UMAP embeddings revealed overall comparable developmental trajectories from immature (IMN) to mature (CTX-MGE and CTX-CGE) GABAergic neuron subtypes between WT and HOM (Figure S3A). Despite overall similarities in inferred lineage flow between WT and HOM mice, the distribution of cell states differed across the trajectory. IMN GABAergic neurons were markedly increased in HOM mice and were positioned at earlier stages of the inferred trajectory (Figure S3B). Notably, IMN GABA neurons and CTX-MGE/CGE neurons formed distinct clusters on the latent time map, supporting clear separation between immature and mature GABAergic populations. Together, these observations suggest that *Scn2a* deficiency may alter the distribution of GABAergic cell states, leading to an expansion of immature neurons.

Scn2a-deficient GABAergic neurons showed disruption in postsynaptic membrane and neurotransmitter activity regulation

Our scVelo analysis demonstrated that an immature neuronal population in the inhibitory lineage is shaped by distinct

transcriptional programs inferred from latent time and driving gene dynamics (Table S3). To investigate cell-type-specific transcriptional changes associated with *Scn2a* deficiency, we performed differential expression analysis across distinct cell types. Significantly differentially expressed genes (DEGs) were identified using thresholds of false discovery rate (FDR) < 0.05 and |log fold change (logFC)| > 0.5. We then quantified the number of DEGs in each class between WT and HOM mice (Fig. 3A, Table S4). This class-level pseudo-bulk approach, aggregating individual nuclei into cell-type groups and performing pairwise differential gene expression analyses between WT and HOM mice within each cell class, enabled us to identify genes and pathways disrupted in the major neuronal subtypes of the mPFC. Among all classes, IT-ET Glut neurons showed the highest number of DEGs (Fig. 3A), indicating a pronounced transcriptional impact of *Scn2a* deficiency in this population, possibly related to *Scn2a*'s high expression in glutamatergic neurons.

To investigate transcriptomic changes within GABAergic neuron subtypes, we subclustered GABA neurons into three major classes: CTX-MGE GABA, CTX-CGE GABA, and IMN GABA (Fig. 3B). To account for differences in IMN GABA cell numbers between genotypes, DE analysis was performed using normalized gene expression per cell. Like the increase in the IMN GABA population in HOM mice compared to WT (Fig. 2), the IMN GABA class exhibited the greatest number of significant DEGs among GABAergic subclasses, followed by CTX-MGE GABA and CTX-CGE GABA neurons (Fig. 3C, D). Notably, 30 DEGs were shared across all three GABAergic classes, including *Pex5l, Nr3c2, Syn3*, and *Slc6a1*, which are involved in synapse regulation. These results suggest that *Scn2a* deficiency may induce both subtype-specific and shared transcriptomic alterations across GABAergic neuron classes.

To uncover the functional implications of DEGs in GABAergic neurons identified above, we performed ClueGO functional enrichment analysis [40] in Cytoscape and identified ontologies related to brain function and neuronal regulation. The ClueGO module visualized enriched gene ontology (GO) terms across biological process (BP), cellular component (CC), and molecular function (MF) networks for DEGs identified in IMN GABA, CTX-MGE GABA, and CTX-CGE GABA (Table S5-6).

In the CTX-MGE GABA class, 133 upregulated DEGs were enriched in GO terms related to the regulation of postsynaptic membrane potential (Fig. 3E). 82 downregulated DEGs were associated with disrupted processes, including regulation of GABAergic synaptic transmission and the voltage-gated potassium channel complex (Fig. 3E). Similarly, in the CTX-CGE GABA class, 101 upregulated DEGs were enriched in postsynaptic density and membrane specialization, while 61 downregulated DEGs were linked to regulation of amine transport and neurotransmitter biosynthetic process (Fig. 3F). For IMN GABA class, 198 upregulated DEGs formed large, enriched networks involved in the regulation of postsynaptic density membrane, action potential, and potassium ion transmembrane transport (Fig. 3G). 43 downregulated DEGs were linked to the regulation of amino acid transport (Fig. 3G).

To identify the genes most affected by *Scn2a* deficiency across mature GABAergic subtypes, we next focused on the 31 genes shared between the CTX-MGE and CTX-CGE GABA classes that were dysregulated. STRING analysis [41] revealed downregulation of GABA transport-related genes (including *Gad1* and *Slc32a1*) and upregulation of synaptic genes (including *Cdh8* and *Syn3*) in HOM (Fig. 3H, Table S7). Given that *Scn2a* is expressed in both CTX-MGE GABA and CTX-CGE GABA neurons (Fig. 1C and D), these results suggest that *Scn2a* deficiency might lead to compensatory upregulation of synaptic genes in mature GABA neurons, resulting in disruption of postsynaptic density regulation and membrane specialization.

Scn2a-deficient glutamatergic neurons have differential gene expression of transcripts involved in synapse transmission and ion transport

Since *Scn2a* is primarily expressed in excitatory neurons (Fig. 1C and D) [2, 14], we next focused on transcriptomic changes in excitatory neurons, whose population sizes remain comparable between WT and HOM. Specifically, we examined whether their gene expression patterns mirrored those observed in inhibitory neurons.

We subclustered the excitatory neuron population in the UMAP and focused on cell types within the IT-ET Glut and NP-CT-L6b Glut class (Fig. 4A). The IT-ET Glut class showed the highest number of DEGs among glutamatergic subtypes in our analysis (Fig. 4B, C). GO enrichment analysis revealed that 205 DEGs upregulated in IT-ET Glut neurons of HOM mice were significantly enriched in action potential regulation and plasma membrane cell adhesion molecules, while 170 downregulated DEGs were associated with amino acid transport and postsynaptic organization (Fig. 4D, Table S5-6). For the NP-CT-L6b Glut class, 110 upregulated DEGs were enriched in nuclear receptor activity, while 54 downregulated genes were linked to glutamate receptor activity (Fig. 4E).

To identify common molecular changes across excitatory neuron subtypes, we performed STRING network analysis on DEGs shared between the IT-ET Glut and NP-CT-L6b Glut classes. This analysis revealed a connected gene network of hub genes implicated in neuronal development, synaptic signaling, and glutamate transmission, including *Neurod6, Nrn1, Grin3a, Slc1a2*, and *Lrrc4c* (Fig. 4F, Table S7). These findings suggest a coordinated dysregulation of core functional pathways in excitatory neurons of HOM mice. The presence of shared DEGs across distinct excitatory classes indicates that *Scn2a* deficiency induces convergent transcriptional changes that may broadly impair glutamatergic signaling in both L2/3 and L4/5 cortical layers. Together with DEG analysis, these results suggest that *Scn2a* loss disrupts key regulatory networks underlying excitatory neuron and cortical function.

Glial cells show differential gene expression of transcripts associated with forebrain neuron development and synapse regulation in response to Scn2a deficiency

We identified DEGs and enriched pathways in non-neuronal cells to assess the transcriptional impact of *Scn2a* deficiency. UMAP subclustering revealed distinct class types corresponding to Astrocytes, OPC-Oligo (oligodendrocyte progenitor cells and oligodendrocytes), Immune (microglia), OEC (olfactory ensheathing cells), and Vascular classes (Fig. 5A). By focusing on the three major glial types: Astrocytes, OPC-Oligo, and Immune cells (microglia), we identified overlapping and unique DEGs. Astrocytes class exhibited the largest number of unique DEGs, followed by OPC-Oligo and Immune classes (Fig. 5B, C).

GO enrichment analysis was then performed for upregulated and downregulated DEGs within each glial class. Among them, Astrocytes showed the most extensive enrichment networks compared to OPC-Oligo and Immune cells (Fig. 5D). In Astrocytes, upregulated genes were associated with the postsynaptic density membrane, suggesting potential alterations in neuron-glia synaptic interactions. Downregulated genes were enriched in pathways related to forebrain neuron differentiation, likely reflecting a disruption in astrocyte-mediated support for neuronal development or maintenance (Fig. 5D). In OPC-Oligo, upregulated DEGs showed enrichment in membrane lipid distribution and neuron migration (Fig. 5E). For microglia, upregulated DEGs were associated with the regulation of actin depolymerization and nerve development (Fig. 5F). Given that *Scn2a* has very limited expression in glial populations, these transcriptomic changes are likely secondary, non-cell-autonomous effects in response to

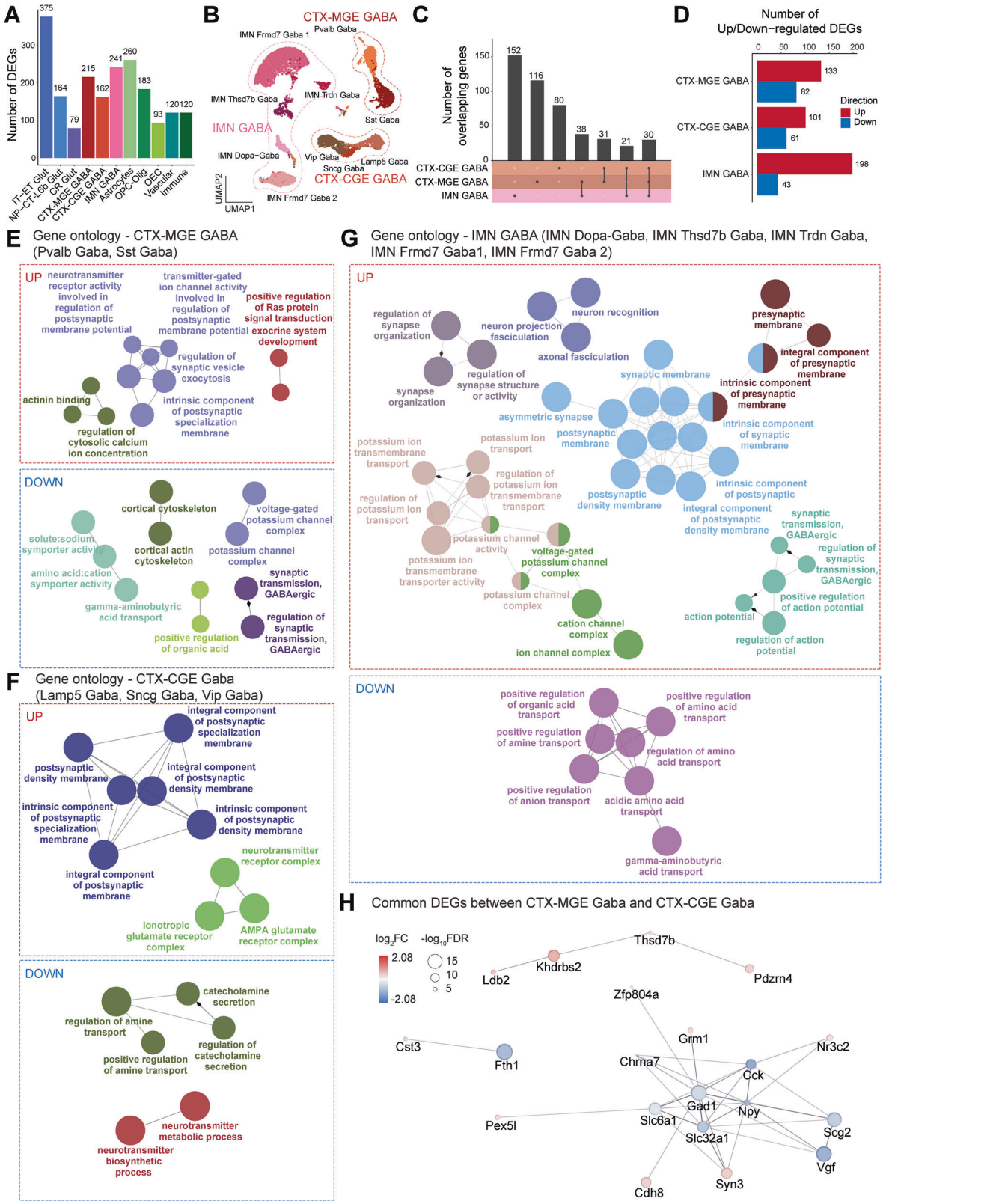


Fig. 3 ***Scn2a*** **deficiency alters ion channel– and neurotransmission-related gene expression in GABAergic neurons. A** Bar plot showing the number of significant DEGs identified in each annotated cell class. **B** UMAP visualization of the GABAergic neuron subset. **C** UpSet plot showing shared and class-specific DEGs across GABAergic neuron classes in HOM compared with WT mice. Rows indicate GABAergic neuron classes, and columns indicate DEG intersections across classes. **D** Bar plot showing the number of upregulated and downregulated DEGs across GABAergic neuron classes. **E**–**G** GO enrichment analyses of upregulated and downregulated DEGs in CTX-MGE GABA neurons (**E**), CTX-CGE GABA neurons (**F**), and IMN GABA neurons (**G**). Black arrows indicate hierarchical relationships among GO terms, whereas terms without arrows indicate similarity- or overlap-based associations. **H** STRING network visualization of shared DEGs between CTX-MGE GABA and CTX-CGE GABA neurons. Node size corresponds to −log10(FDR), and color indicates the direction of gene-expression change. Red, upregulated; blue, downregulated.

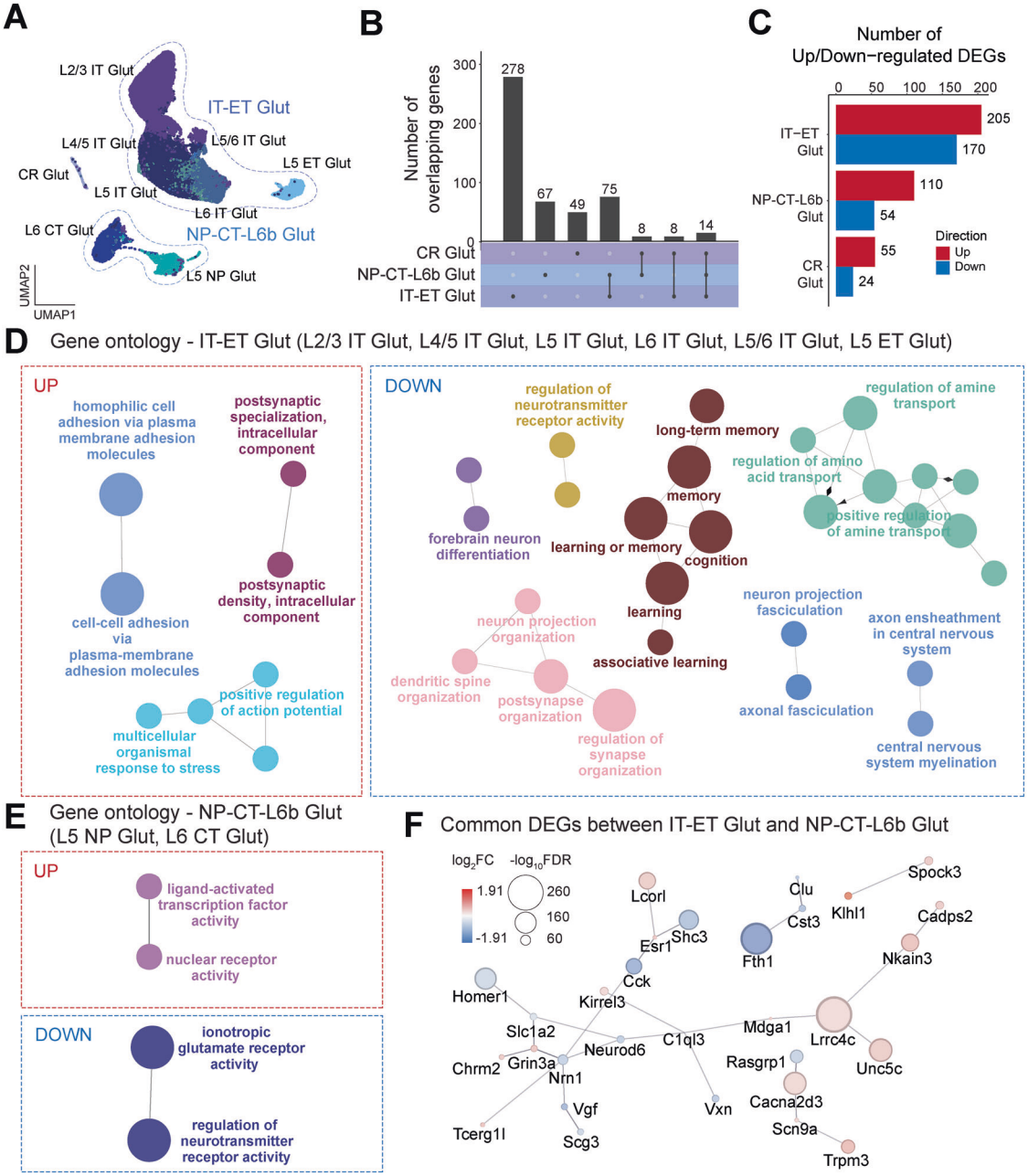


Fig. 4 ***Scn2a*** **deficiency alters synaptic organization and neuronal regulatory gene programs in glutamatergic neurons. A** UMAP visualization of the glutamatergic neuron subset. **B** UpSet plot showing shared and class-specific DEGs across glutamatergic neuron classes in HOM compared with WT mice. Rows indicate glutamatergic neuron classes, and columns indicate DEG intersections across classes. **C** Bar plot showing the number of upregulated and downregulated DEGs across glutamatergic neuron classes. **D**, **E** GO enrichment analyses of upregulated and downregulated DEGs in IT-ET Glut neurons (**D**) and NP-CT-L6b Glut neurons (**E**). Black arrows indicate hierarchical relationships among GO terms, whereas terms without arrows indicate similarity- or overlap-based associations. **F** STRING network visualization of DEGs shared between IT-ET Glut and NP-CT-L6b Glut neurons, analyzed using Cytoscape.

Scn2a deficiency. Notably, astrocytes appeared to be the most transcriptionally affected glial cell type, highlighting their potential role in modulating neuronal function following *Scn2a* loss.

Neuronal modulation genes were restored by FlpO genetic rescue

From our analysis, we identified cell-type-specific transcriptomic alterations in glutamatergic and GABAergic neurons caused by *Scn2a* deficiency and wanted to explore whether re-expression of *Scn2a* in adulthood could reverse these transcriptional changes. We performed a genetic rescue experiment by systemically administering AAV-PHP.eB-FlpO via tail vein injection in adult HOM mice, which excises the gene trap cassette and partially restores *Scn2a* expression [17]. Transcriptomic analyses in HOM-FlpO mice revealed that adult *Scn2a* restoration did not reduce the expanded IMN GABA population (Fig. 6A) nor their earlier latent time characteristics (data not shown). This could be due to developmental alterations in cell fate and cellular composition being difficult to reverse once established.

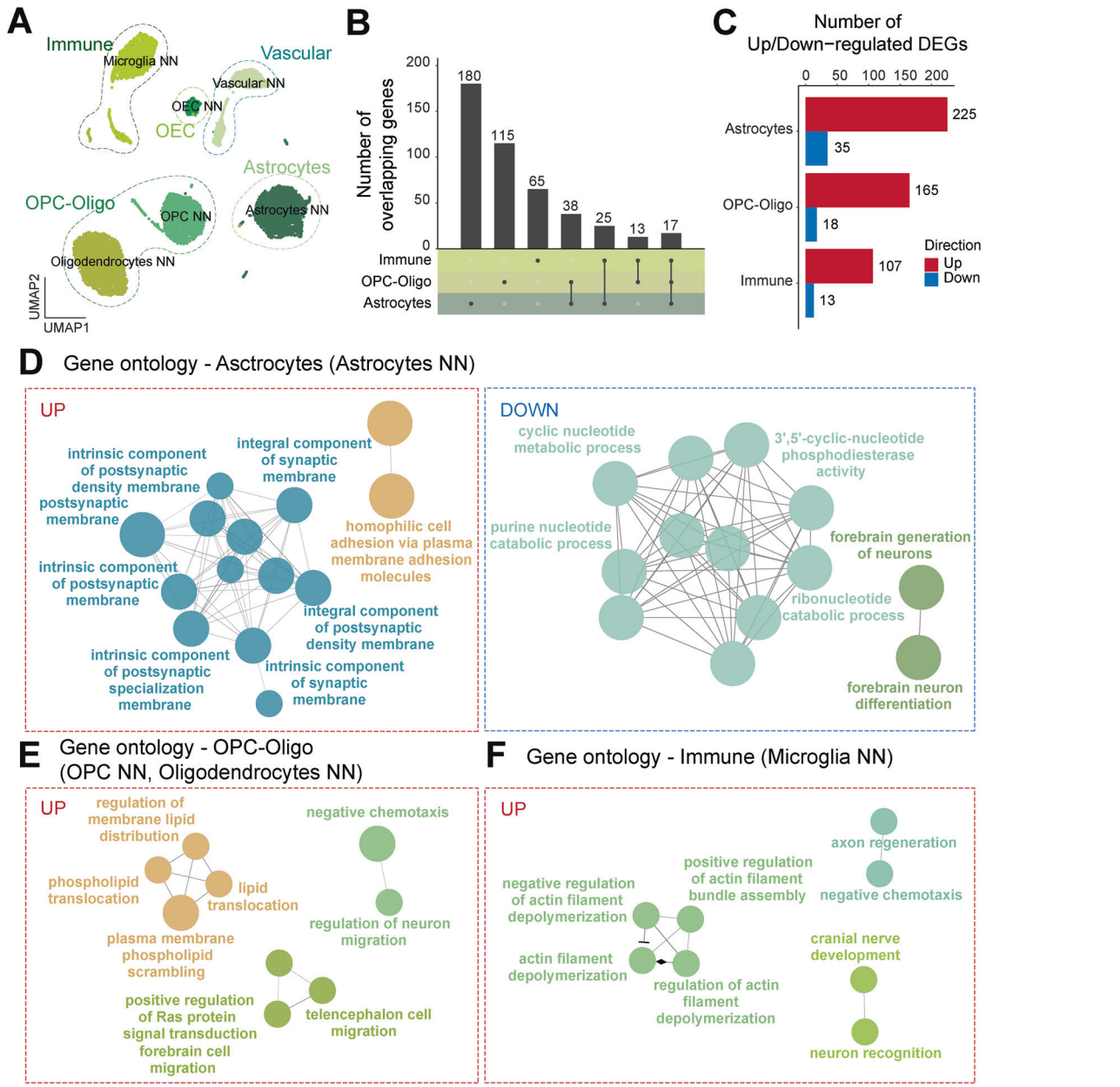


Fig. 5 Glial and immune cells in HOM mice show altered membrane- and synapse-related transcriptional programs. A UMAP visualization of the non-neuronal cell subset. **B** UpSet plot showing shared and cell type–specific DEGs across major glial/non-neuronal populations, including astrocytes, OPC-Oligo cells, and immune/microglial cells, in HOM compared with WT mice. Rows indicate cell types, and columns indicate DEG intersections across cell types. **C** Bar plot showing the number of upregulated and downregulated DEGs across glial/non-neuronal cell types. **D**–**F** GO enrichment analyses of DEGs in astrocytes (**D**), OPC-Oligo cells (**E**), and immune/microglial cells (**F**). Black arrows indicate hierarchical relationships among GO terms, black bars indicate negative regulatory relationships, and terms without arrows indicate similarity- or overlap-based associations.

To examine relationships among DEGs in WT and HOM mice and the effects of FlpO-mediated *Scn2a* restoration, we applied CellPhoneDB v5. This bioinformatics framework infers cell–cell communication from single-cell transcriptomic data using curated, experimentally supported ligand–receptor interactions [42]. The latest version of CellPhoneDB incorporates interactions mediated by nonpeptidic ligands, including neurotransmitters and small molecules targeting G protein–coupled receptors (GPCRs), enabling broader coverage of signaling interactions across neural cell types. Using this approach, we observed that HOM mice exhibited a higher number of predicted cell–cell interactions than WT mice. Notably, this increase was attenuated following FlpO-mediated adult restoration of *Scn2a* expression (Fig. 6B, Table S8).

To further assess cell-type-specific communication, we analyzed the number of interactions by source and target neuronal subtypes. Intriguingly, *Scn2a* restoration in HOM mice broadly reduced interactions across all GABAergic and glutamatergic cell pairings (GABA-GABA, GABA-Glut, Glut-GABA, and Glut-Glut) (Fig. 6C). This finding implies that adult *Scn2a* expression rescue may partially normalize existing aberrant cell-cell communication patterns in HOM mice.

Finally, we conducted differential expression analysis between HOM-FlpO and HOM to uncover gene expression alterations driven by adult *Scn2a* restoration. We focused on DEGs showing opposite expression changes between WT and HOM, and between HOM and HOM-FlpO, in glutamatergic and GABAergic neurons.

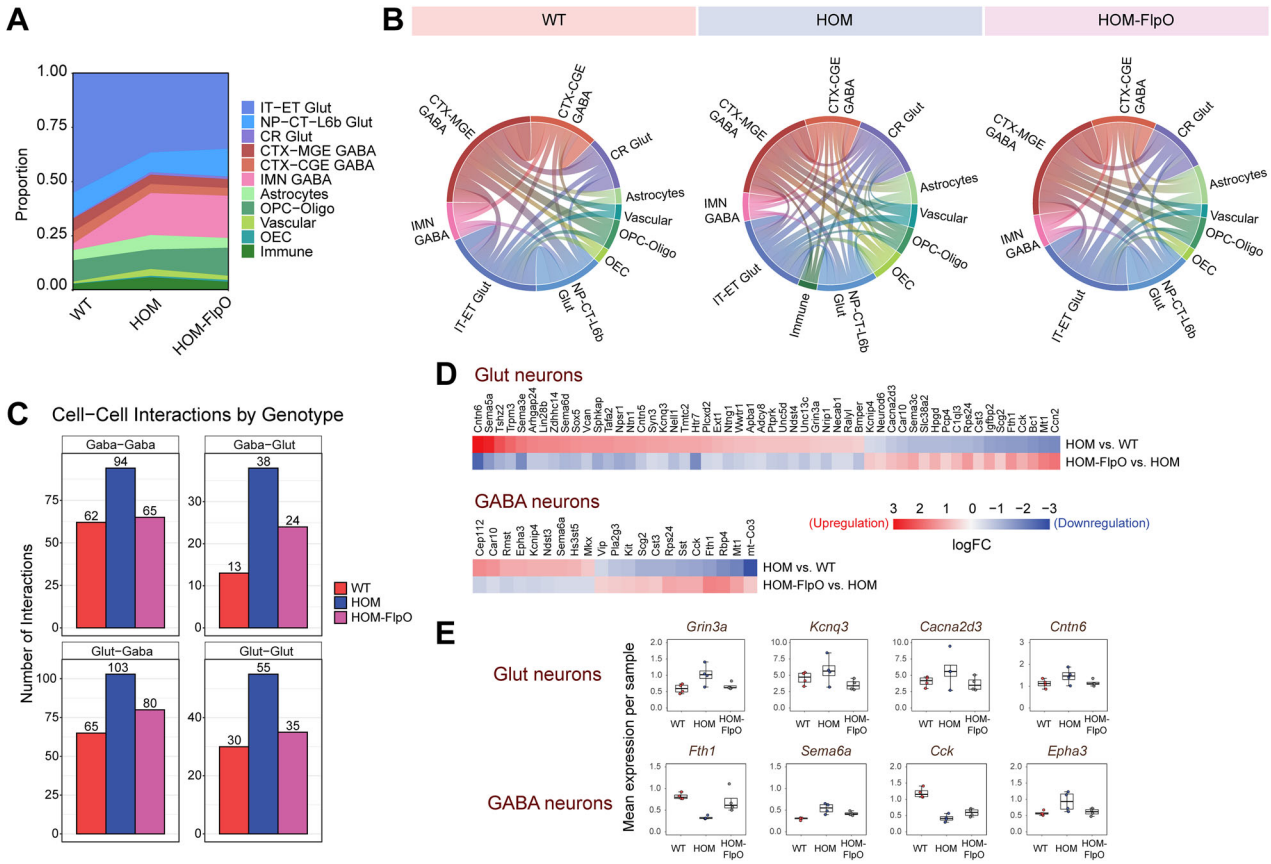


Fig. 6 FlpO-mediated *Scn2a* restoration reduces predicted cell–cell communication and partially normalizes gene expression in *Scn2a*-deficient mice. A Stacked area plot showing the relative proportions of neuronal and non-neuronal cell classes across WT, HOM-Control, and HOM-FlpO groups. The IMN GABA population remained present in both HOM-Control and HOM-FlpO mice. **B** Circos plots showing predicted cell–cell communication networks in WT, HOM, and HOM-FlpO mice based on CellPhoneDB v5 analysis. **C** Bar plot showing the total number of predicted interactions among GABAergic and glutamatergic neuron pairs, including GABA–GABA, GABA–Glut, Glut–GABA, and Glut–Glut interactions, across WT, HOM-Control, and HOM-FlpO groups. **D** Heatmap of DEGs across comparison groups, highlighting genes altered in HOM versus WT and partially normalized in HOM-FlpO versus HOM. Red indicates upregulated genes, and blue indicates downregulated genes. **E** Mean expression levels of representative rescued genes in glutamatergic and GABAergic neurons, including genes associated with synaptic adhesion, neurotransmission, and ion channel function. Grin3a glutamate ionotropic receptor NMDA type subunit 3A, Kcnq3 potassium voltage-gated channel subfamily Q member 3, Cacna2d3 calcium voltage-gated channel auxiliary subunit alpha2delta 3, Cntn6 contactin 6, Fth1 ferritin heavy chain 1, Sema6a semaphorin 6A, Cck cholecystokinin, Epha3 EPH receptor A3.

This analysis identified 54 'rescued genes' in glutamatergic neurons (i.e., IT-ET-Glut, NP-CT-Glut, CR Glut) and 21 in GABAergic neurons (i.e., CTX-MGE Gaba, CTX-CGE Gaba, IMN Gaba) (Fig. 6D, E, Table S9). Notably, genes such as *Grin3a*, *Kcnq3*, *Cacna2d3*, and *Cntn6* in glutamatergic neurons, and *Fth1*, *Sema6a*, *Cck*, and *Epha3* in GABAergic neurons are linked to synaptic signaling, circuit connectivity, and overall cellular homeostasis. These findings suggest that restoring the *Scn2a* gene in adulthood can reverse certain disease-associated transcriptomic changes.

DISCUSSION

In this study, we employed single-nucleus RNA sequencing to define the cell-type-specific transcriptional landscape of the medial prefrontal cortex (mPFC) in a mouse model of *Scn2a* deficiency. We profiled transcriptomic changes in *Scn2a* homozygous gene trap (HOM) mice and wild-type (WT) controls. By adopting MapMyCells from the Allen Brain Institute [35], cell identities were annotated to reveal major classes, including IT-ET Glut, NP-CT-L6b Glut, CTX-MGE GABA, CTX-CGE GABA, IMN GABA, and non-neuronal cells. Notably, we observed a marked increase in the proportion of IMN GABA neurons in the mPFC of *Scn2a* HOM mice. These cells expressed neuronal development-related genes, consistent with an immature phenotype. Differential gene expression analysis showed that *Scn2a* deficiency alters genes related to synaptic transmission and voltage-gated potassium channels in GABAergic neurons (Fig. 3), while glutamatergic neurons are enriched for pathways involving membrane potential and glutamate receptor signaling (Fig. 4). These transcriptomic alterations in different cell types may contribute to neuronal hyperexcitability and social deficits observed in the *Scn2a*-deficient mouse model [28].

The increased proportion of IMN GABA neurons observed in our dataset may reflect early developmental consequences of *Scn2a* deficiency; however, whether this represents a cell-autonomous effect within GABAergic neurons or their progenitors, or a secondary non-cell-autonomous response to altered network activity, remains to be determined. A recent study suggested that loss of *SCN2A* function impairs both excitatory and inhibitory neurogenesis, leading to developmental imbalance through elevated sonic hedgehog (SHH) signaling [50]. Consistent with this interpretation, gene ontology analysis revealed enrichment of neuron projection and axonal fasciculation pathways in IMN GABA neurons (Fig. 3G), but downregulation in IT-ET glut neurons (Fig. 4D). This indicates that sodium channel deficiency differentially reshapes neurodevelopmental programs in a cell–type–dependent

manner. Together with our results, these findings underscore the central role of *Scn2a* in guiding neurogenesis.

The increased population of IMN GABA neurons is marked by canonical genes associated with early GABAergic neuron development, such as *Meis2, Trdn, Frmd7*, and *Thsd7b* [49, 53–56] (Fig. 1E). In particular, *Meis2* is a key transcription factor involved in neurodevelopment, cell fate specification [57, 58], and GABAergic neuron differentiation [59]. We observed that IMN GABA neurons persist as a distinct population in the mPFC of HOM mice, suggesting that these cells may represent a terminal fate rather than a transient stage in further differentiation. Our findings suggest that *Scn2a* deficiency may interfere with this migratory or maturational process, leading to the retention of IMN GABA neurons in inappropriate brain regions. Nevertheless, the lack of comprehensive protein quantification of *Meis2*+ GABA neurons in situ is a limitation of this study. Further longitudinal studies across developmental time points, as well as functional validation, are necessary to determine whether *Scn2a* loss disrupts interneuron migration or delays maturation.

In addition to IMN GABA neurons, glutamatergic neurons and glial cells also exhibit significant changes in response to *Scn2a* deficiency. In glutamatergic neurons, gene ontology analysis indicates upregulation of genes involved in action potential regulation and postsynaptic regulation. The result is in line with our data on pyramidal neuronal hyperexcitability [17] and disrupted excitatory/inhibitory postsynaptic currents in *Scn2a*-deficient mice [28]. Interestingly, genes related to cognitive functions such as learning and memory are downregulated, consistent with clinical presentations in ASD patients. This is accompanied by downregulation of genes for neurotransmitters, neuron projection, and myelination, which sheds light on potential underlying mechanisms leading to ASD symptoms. Non-neuronal cells were also altered in the HOM mice, with a moderate increase in astrocyte, microglia, and vascular cell populations (Fig. 2). This phenotype further suggests a global disruption of cellular lineages during HOM mouse development caused by *Scn2a* deficiency. Astrocytes, the most affected non-neuronal cell type, exhibited upregulation of genes involved in synaptic regulation and downregulation of genes associated with nucleotide metabolism. These findings suggest that the expanded astrocyte population actively responds to the pathological brain environment in HOM mice, potentially through interactions with nearby neurons at the tripartite synapse. Conversely, metabolic support from astrocytes may be depleted due to reduced biosynthetic capacity resulting from persistent neuronal hyperactivity in the region, thereby lowering the astrocytes' energy-buffering capacity to sustain neurons. Intriguing hypotheses arising from the sequencing results could be tested in future follow-up experiments to uncover the underlying cellular mechanisms of *Scn2a* deficiency and to deepen our understanding of the pathophysiology of genetic ASD.

Together, our snRNA-seq results reveal changes in cellular composition and gene expression resulting from *Scn2a* deficiency. We found that IMN GABA neurons within the *Scn2a*-deficient mPFC exhibited a distinct transcriptional state among GABAergic neuronal subtypes. Differentially expressed genes in both GABAergic and glutamatergic neurons highlighted ontologies related to ion channels and synapse organization. *Scn2a* gene restoration affected cellular interactions across cell types and altered gene expression in both GABAergic neurons and glutamatergic neurons. Our results provide a transcriptomic framework for investigating the molecular effects of *Scn2a* loss-of-function across different cell types, thereby informing disease mechanisms and interventions [60, 61].

DATA AVAILABILITY

All data supporting the findings of this study are included in the article and its Supplementary Information or are available from the corresponding author upon request.

REFERENCES

1. Shi X, Yasumoto S, Kurahashi H, Nakagawa E, Fukasawa T, Uchiya S, et al. Clinical spectrum of SCN2A mutations. Brain Dev. 2012;34:541–5.
2. Meisler MH, Hill SF, Yu W. Sodium channelopathies in neurodevelopmental disorders. Nat Rev Neurosci. 2021;22:152–66.
3. Gazina EV, Leaw BT, Richards KL, Wimmer VC, Kim TH, Aumann TD, et al. 'Neonatal' Nav1.2 reduces neuronal excitability and affects seizure susceptibility and behaviour. Hum Mol Genet. 2015;24:1457–68.
4. Alsaloum M, Dib-Hajj SD, Page DA, Ruben PC, Krainer AR, Waxman SG. Voltage-gated sodium channels in excitable cells as drug targets. Nat Rev Drug Discov. 2025;24:358–78.
5. Nelson AD, Catalfio AM, Gupta JP, Min L, Caballero-Floran RN, Dean KP, et al. Physical and functional convergence of the autism risk genes Scn2a and Ank2 in neocortical pyramidal cell dendrites. Neuron. 2024;112:1133–49. e6.
6. Spratt PWE, Ben-Shalom R, Keeshen CM, Burke KJ Jr., Clarkson RL, Sanders SJ, et al. The autism-associated gene Scn2a contributes to dendritic excitability and synaptic function in the prefrontal cortex. Neuron. 2019;103:673–85. e5.
7. Satterstrom FK, Kosmicki JA, Wang J, Breen MS, De Rubeis S, An JY, et al. Large-scale exome sequencing study implicates both developmental and functional changes in the neurobiology of autism. Cell. 2020;180:568–84. e23.
8. Baasch AL, Huning I, Gilissen C, Klepper J, Veltman JA, Gillessen-Kaesbach G, et al. Exome sequencing identifies a de novo SCN2A mutation in a patient with intractable seizures, severe intellectual disability, optic atrophy, muscular hypotonia, and brain abnormalities. Epilepsia. 2014;55:e25–9.
9. Zhou X, Feliciano P, Shu C, Wang T, Astrovskaya I, Hall JB, et al. Integrating de novo and inherited variants in 42,607 autism cases identifies mutations in new moderate-risk genes. Nat Genet. 2022;54:1305–19.
10. Codina-Sola M, Rodriguez-Santiago B, Homs A, Santoyo J, Rigau M, Aznar-Lain G, et al. Integrated analysis of whole-exome sequencing and transcriptome profiling in males with autism spectrum disorders. Mol Autism. 2015;6:21.
11. Weiss LA, Escayg A, Kearney JA, Trudeau M, MacDonald BT, Mori M, et al. Sodium channels SCN1A, SCN2A and SCN3A in familial autism. Mol Psychiatry. 2003;8:186–94.
12. Clatot J, Thompson CH, Sotardi S, Jiang J, Trivisano M, Balestrini S, et al. Rare dysfunctional SCN2A variants are associated with malformation of cortical development. Epilepsia. 2025;66:914–28.
13. Asadollahi R, Delvendahl I, Muff R, Tan G, Rodriguez DG, Turan S, et al. Pathogenic SCN2A variants cause early-stage dysfunction in patient-derived neurons. Hum Mol Genet. 2023;32:2192–204.
14. Sanders SJ, Campbell AJ, Cottrell JR, Moller RS, Wagner FF, Auldridge AL, et al. Progress in understanding and treating SCN2A-Mediated disorders. Trends Neurosci. 2018;41:442–56.
15. Catterall WA. Sodium channels, inherited epilepsy, and antiepileptic drugs. Annu Rev Pharmacol Toxicol. 2014;54:317–38.
16. Eaton M, Zhang J, Ma Z, Park AC, Lietzke E, Romero CM, et al. Generation and basic characterization of a gene-trap knockout mouse model of Scn2a with a substantial reduction of voltage-gated sodium channel Na(v) 1.2 expression. Genes Brain Behav. 2021;20:e12725.
17. Zhang J, Chen X, Eaton M, Wu J, Ma Z, Lai S, et al. Severe deficiency of the voltage-gated sodium channel Na(V)1.2 elevates neuronal excitability in adult mice. Cell Rep. 2021;36:109495.
18. Grossmann T. The role of medial prefrontal cortex in early social cognition. Front Hum Neurosci. 2013;7:340.
19. Menon V, D'Esposito M. The role of PFC networks in cognitive control and executive function. Neuropsychopharmacology. 2022;47:90–103.
20. Bhattacherjee A, Zhang C, Watson BR, Djekidel MN, Moffitt JR, Zhang Y. Spatial transcriptomics reveals the distinct organization of mouse prefrontal cortex and neuronal subtypes regulating chronic pain. Nat Neurosci. 2023;26:1880–93.
21. Bhattacherjee A, Djekidel MN, Chen R, Chen W, Tuesta LM, Zhang Y. Cell type-specific transcriptional programs in mouse prefrontal cortex during adolescence and addiction. Nat Commun. 2019;10:4169.
22. Mao X, Staiger JF. Multimodal cortical neuronal cell type classification. Pflug Arch. 2024;476:721–33.
23. Euston DR, Gruber AJ, McNaughton BL. The role of medial prefrontal cortex in memory and decision making. Neuron. 2012;76:1057–70.
24. Lanooij SD, Eisel ULM, Drinkenburg W, van der Zee EA, Kas MJH. Influencing cognitive performance via social interactions: a novel therapeutic approach for brain disorders based on neuroanatomical mapping?. Mol Psychiatry. 2023;28:28–33.
25. Porcelli S, Van Der Wee N, van der Werff S, Aghajani M, Glennon JC, van Heukelum S, et al. Social brain, social dysfunction and social withdrawal. Neurosci Biobehav Rev. 2019;97:10–33.
26. Xu P, Chen A, Li Y, Xing X, Lu H. Medial prefrontal cortex in neurological diseases. Physiol Genomics. 2019;51:432–42.
27. Shang Z, Zhang X. Postnatal critical-period brain plasticity and neurodevelopmental disorders: revisited circuit mechanisms. J Genet Genomics. 2025;52:1177–88.

28. Zhang J, Eaton M, Chen X, Zhao Y, Kant S, Deming BA, et al. Restoration of excitation/inhibition balance enhances neuronal signal-to-noise ratio and rescues social deficits in autism-associated *Scn2a*-deficiency. bioRxiv:2025.03.04.641498 [Preprint]. 2025. Available from: https://www.biorxiv.org/content/10.1101/2025.03.04.641498v1.
29. Wager-Miller J, Murphy Green M, Shafique H, Mackie K. Collection of frozen rodent brain regions for downstream analyses. JoVE. 2020;158:e60474.
30. Wolf FA, Angerer P, Theis FJ. SCANPY: large-scale single-cell gene expression data analysis. Genome Biol. 2018;19:15.
31. Wolock SL, Lopez R, Klein AM. Scrublet: computational identification of cell doublets in single-cell transcriptomic data. Cell Syst. 2019;8:281–91. e9.
32. Stuart T, Butler A, Hoffman P, Hafemeister C, Papalexi E, Mauck WM 3rd, et al. Comprehensive integration of single-cell data. Cell. 2019;177:1888–902. e21.
33. Butler A, Hoffman P, Smibert P, Papalexi E, Satija R. Integrating single-cell transcriptomic data across different conditions, technologies, and species. Nat Biotechnol. 2018;36:411–20.
34. Marsh S. scCustomize: custom visualizations & functions for streamlined analyses of single cell sequencing. 2025. https://github.com/samuel-marsh/scCustomize.
35. Yao Z, van Velthoven CTJ, Kunst M, Zhang M, McMillen D, Lee C, et al. A high-resolution transcriptomic and spatial atlas of cell types in the whole mouse brain. Nature. 2023;624:317–32.
36. Daniel SF, Lee C, Mollenkopf T, Lee M, Arbuckle J, Fiabane E, et al. High-performance mapping of unlabeled cell-by-gene data to reference brain taxonomies. bioRxiv:2026.03.06.710160 [Preprint]. 2026. Available from: https://www.biorxiv.org/content/10.64898/2026.03.06.710160v1.
37. Zappia L, Oshlack A. Clustering trees: a visualization for evaluating clusterings at multiple resolutions. GigaScience. 2018;7:giy083.
38. Bergen V, Lange M, Peidli S, Wolf FA, Theis FJ. Generalizing RNA velocity to transient cell states through dynamical modeling. Nat Biotechnol. 2020;38:1408–14.
39. La Manno G, Soldatov R, Zeisel A, Braun E, Hochgerner H, Petukhov V, et al. RNA velocity of single cells. Nature. 2018;560:494–8.
40. Bindea G, Mlecnik B, Hackl H, Charoentong P, Tosolini M, Kirilovsky A, et al. ClueGO: a cytoscape plug-in to decipher functionally grouped gene ontology and pathway annotation networks. Bioinformatics. 2009;25:1091–3.
41. Szklarczyk D, Kirsch R, Koutrouli M, Nastou K, Mehryary F, Hachilif R, et al. The STRING database in 2023: protein-protein association networks and functional enrichment analyses for any sequenced genome of interest. Nucleic Acids Res. 2023;51:D638–D46.
42. Troule K, Petryszak R, Cakir B, Cranley J, Harasty A, Prete M, et al. CellPhoneDB v5: inferring cell-cell communication from single-cell multiomics data. Nat Protoc. 2025;20:3412–40.
43. Zeng Z, Ma Y, Hu L, Tan B, Liu P, Wang Y, et al. OmicVerse: a framework for bridging and deepening insights across bulk and single-cell sequencing. Nat Commun. 2024;15:5983.
44. Bankhead P, Loughrey MB, Fernandez JA, Dombrowski Y, McArt DG, Dunne PD, et al. QuPath: open source software for digital pathology image analysis. Sci Rep. 2017;7:16878.
45. Shin W, Kweon H, Kang R, Kim D, Kim K, Kang M, et al. Scn2a haploinsufficiency in mice suppresses hippocampal neuronal excitability, excitatory synaptic drive, and long-term potentiation, and spatial learning and memory. Front Mol Neurosci. 2019;12:145.
46. Yamagata T, Ogiwara I, Mazaki E, Yanagawa Y, Yamakawa K. Nav1.2 is expressed in caudal ganglionic eminence-derived disinhibitory interneurons: mutually exclusive distributions of Nav1.1 and Nav1.2. Biochem Biophys Res Commun. 2017;491:1070–6.
47. Obernier K, Alvarez-Buylla A. Neural stem cells: origin, heterogeneity and regulation in the adult mammalian brain. Development. 2019;146:dev156059.
48. Lim DA, Alvarez-Buylla A. The adult ventricular-subventricular zone (V-SVZ) and olfactory bulb (OB) neurogenesis. Cold Spring Harb Perspect Biol. 2016;8:a018820.
49. van Velthoven CTJ, Gao Y, Kunst M, Lee C, McMillen D, Chakka AB, et al. Transcriptomic and spatial organization of telencephalic GABAergic neurons. Nature. 2025;647:143–56.
50. Uy JA, Dargaei Z, Geahchan S, Botler L, Pan Y, Brown CO, et al. The sodium channel SCN2A regulates cortical excitatory and inhibitory neurogenesis. Nat Commun 2026.
51. Setty M, Kiseliovas V, Levine J, Gayoso A, Mazutis L, Pe'er D. Characterization of cell fate probabilities in single-cell data with Palantir. Nat Biotechnol. 2019;37:451–60.
52. Trapnell C, Cacchiarelli D, Grimsby J, Pokharel P, Li S, Morse M, et al. The dynamics and regulators of cell fate decisions are revealed by pseudotemporal ordering of single cells. Nat Biotechnol. 2014;32:381–6.
53. Marty I. Triadin: a multi-protein family for which purpose? Cell Mol Life Sci. 2004;61:1850–3.
54. Betts-Henderson J, Bartesaghi S, Crosier M, Lindsay S, Chen HL, Salomoni P, et al. The nystagmus-associated FRMD7 gene regulates neuronal outgrowth and development. Hum Mol Genet. 2010;19:342–51.
55. Pu J, Dai S, Gao T, Hu J, Fang Y, Zheng R, et al. Nystagmus-related FRMD7 gene influences the maturation and complexities of neuronal processes in human neurons. Brain Behav. 2019;9:e01473.
56. Yao Z, Lin A, Yi Y, Shen W, Zhang J, Luo P. THSD7B mutation induces platinum resistance in small cell lung cancer patients. Drug Des Devel Ther. 2022;16:1679–95.
57. Dupacova N, Antosova B, Paces J, Kozmik Z. Meis homeobox genes control progenitor competence in the retina. Proc Natl Acad Sci USA. 2021;118:e2013136118.
58. Agoston Z, Schulte D. Meis2 competes with the Groucho co-repressor Tle4 for binding to Otx2 and specifies tectal fate without induction of a secondary midbrain-hindbrain boundary organizer. Development. 2009;136:3311–22.
59. Bragado Alonso S, Reinert JK, Marichal N, Massalini S, Berninger B, Kuner T, et al. An increase in neural stem cells and olfactory bulb adult neurogenesis improves discrimination of highly similar odorants. EMBO J. 2019;38:e98791.
60. Robinson M, Wettschurack K, Halurkar MS, Chen X, Zhang Z, Zhang J, et al. Precision medicine for sodium channelopathy-related autism and epilepsy. Trends Mol Med. 2026.
61. Yang Y. What we can learn from the first personalized CRISPR-treated baby to tackle genetic brain disorders. Neuron 2025;113:3697–702.

AUTHOR CONTRIBUTIONS

Y-EY, PM, and ZT implemented the codes, analyzed the data, and drove the study design. Y-EY and ZZ wrote and revised the manuscript. Y-EY, JZ, XC, MR, ME, BD, and MH performed wet lab experiments. HK, ZZ, LCD, BJ, HG, NL, YL, JK, CY, and PB supported data analysis. YY supervised this project. All authors reviewed the manuscript.

FUNDING

Research reported in this study was supported by the National Institutes of Neurological Disorders and Stroke (NINDS) of the National Institutes of Health under award numbers R01NS117585 and R01NS123154. This work was also supported by the Hodgkin-Huxley Research Grant from the FamilieSCN2A Foundation. Data analysis was supported by the Simon Comprehensive Cancer Center (Grant P30CA082709), Purdue University Institute for Cancer Research (Grant P30CA023168), and the Walther Cancer Foundation.

COMPETING INTERESTS

The authors declare no competing interests.

ADDITIONAL INFORMATION

Supplementary information The online version contains supplementary material available at https://doi.org/10.1038/s41398-026-04348-0.

Correspondence and requests for materials should be addressed to Yang Yang.

Reprints and permission information is available at http://www.nature.com/reprints

Publisher's note Springer Nature remains neutral with regard to jurisdictional claims in published maps and institutional affiliations.

Open Access This article is licensed under a Creative Commons Attribution-NonCommercial-NoDerivatives 4.0 International License, which permits any non-commercial use, sharing, distribution and reproduction in any medium or format, as long as you give appropriate credit to the original author(s) and the source, provide a link to the Creative Commons licence, and indicate if you modified the licensed material. You do not have permission under this licence to share adapted material derived from this article or parts of it. The images or other third party material in this article are included in the article's Creative Commons licence, unless indicated otherwise in a credit line to the material. If material is not included in the article's Creative Commons licence and your intended use is not permitted by statutory regulation or exceeds the permitted use, you will need to obtain permission directly from the copyright holder. To view a copy of this licence, visit http://creativecommons.org/licenses/by-nc-nd/4.0/.

© The Author(s) 2026